aerospace

MDPI

Article

Numerical Simulation of Unsteady Fluid Parameters for Maglev Flight Wind Tunnel Design

Cheng Fu [1,2], Xinglong Gao [1,2,*], Yunqiang Sun [1,2], Jie Kou [1,2], Dachuan Xu [1,2] and Jingxiang Chen [1,2]

[1] State Key Laboratory of Aerodynamics of China Aerodynamics Research and Development Center, Mianyang 621000, China
[2] Facility Design and Instrumentation Institute, China Aerodynamics Research and Development Center, Mianyang 621000, China
* Correspondence: gaoxinglong@cardc.cn; Tel.: +86-8162464138

Abstract: The maglev flight tunnel is a novel conceptual aerodynamics test facility, in which the complicated aerodynamic characteristics caused by the high-speed translation of a moving model in a long, straight, closed tunnel, and wave propagation and aero-structure single-way coupling problems can be investigated. The unsteady characteristics originating from a high-speed model in the maglev flight tunnel were investigated and evaluated with regard to aero–structure coupling. The new conservation element and solution element method was used to solve the 3-D compressible fluid surrounding a moving model in a tunnel, and the variations in the aerodynamic parameters, wave propagation characteristics, and pressure distribution in the tunnel were obtained. The results provide support for key technical problems, such as a wave-absorbing construction design of the maglev flight wind tunnel.

Keywords: maglev flight tunnel; fluid structure interaction; unsteady aerodynamics; conservation element and solution element method; numerical simulation

check for updates

Citation: Fu, C.; Gao, X.; Sun, Y.; Kou, J.; Xu, D.; Chen, J. Numerical Simulation of Unsteady Fluid Parameters for Maglev Flight Wind Tunnel Design. *Aerospace* **2023**, *10*, 34. https://doi.org/10.3390/aerospace10010034

Received: 9 October 2022
Revised: 21 December 2022
Accepted: 28 December 2022
Published: 31 December 2022

Copyright: © 2022 by the authors. Licensee MDPI, Basel, Switzerland. This article is an open access article distributed under the terms and conditions of the Creative Commons Attribution (CC BY) license (https://creativecommons.org/licenses/by/4.0/).

1. Introduction

In the aerospace field, the development of various types of advanced military and civil aviation vehicles requires significant changes in national security and social economics. Simultaneously, many new aerodynamic problems require breakthroughs [1]. Basic and frontier problems such as accurate high-speed aerodynamic forecasting and integration design, turbulent drag reduction, boundary layer rotation, and ground effects are strongly dependent on wind tunnel testing, imposing greater requirements for the flow dynamics, low disturbance properties, and special simulation capabilities of wind tunnels than before [2]. Therefore, it is increasingly difficult for conventional wind tunnel equipment to meet the increased need for special aerodynamic testing [3]. In addition, within the research field of advanced railway traffic, railway technology such as magnetic vacuum–pipeline hypervelocity trains have been incorporated into the Chinese "13th Five-Year Plan" priority research and development program. The vacuum–pipeline train faces a range of complex aerodynamic problems, such as shock boundary layer disturbances, supersonic aerodynamic drag reduction, shock reflection in the pipe, and the piston effect, which must be researched using wind tunnel testing [4]. Currently, traditional supersonic wind tunnels are limited by insufficient simulation authenticity resulting from the size of the test segment (length and area of the transect) and relative movement of the air flow. The aerodynamic properties of aerospace vehicle or hypervelocity train motion models and their power, thermal, structure, and control coupling effects in restricted spaces are difficult to solve in traditional supersonic wind tunnels [5–8].

The concept of a "flight wind tunnel" was first proposed by American researchers in the 1990s. Unlike previous wind tunnels, this has a special operation mode and better "moving model–static wind" characteristics. The NASA Langley Research Center began to

focus on this entirely new ground-testing equipment early on and called it the High-Lift Flight Tunnel [9]. Three key research projects were carried out and a plan to develop the technology was demonstrated; however, no significant progress has yet been made, due to the high levels of difficulty associated with the key technologies of the design and construction.

The maglev flight tunnel is a new concept in wind tunnel equipment, which uses the concept of a vacuum–pipeline train combined with the moving model test method. The rationale is to install a maglev-driven model in a long, straight, closed pipe. The system uses electromagnetic suspension, traction, and directional technology to drive a high-speed model to simulate the physical movement processes of various types of aircraft and high-speed trains. By constructing a test state of "moving model–static wind" that is close to the real flight environment and moving characteristics of the test models, the maglev flight tunnel can satisfy the aerodynamic testing needs of aerospace vehicles and high-speed trains under the wide Mach and wide Reynolds number ranges, low noise, low turbulence intensity, high vacuum (high altitude), special gas medium, and restricted space conditions, along with interdisciplinary problems [3,4].

A test model in the maglev flight wind tunnel is driven by a high-speed maglev technique to control its acceleration, uniform speed, and deceleration in the enclosed pipe. By changing the motion of the model by implementing high-precision adjustment and control of the Mach number, the rapid acceleration or deceleration process of the model and the aerodynamics of the sharp speed change phenomenon can be simulated in the tunnel. During testing, the aerodynamic force and acoustic wave propagation generated by the high-speed movement of the model in the wind tunnel are very complex. Simultaneously, there are interactions between the aerodynamic characteristics and structure of the model and maglev platform during the high-speed movement of the model in the closed pipe, which produces a fluid–structure coupling problem [10]. The traditional computational fluid dynamics (CFD) simulation method has some limitations when dealing with coupling problems under high-speed motion in moving models. The dynamic model test process must be numerically simulated using the fluid structure interaction (FSI) method combined with moving mesh technology, and the aerodynamic characteristics of the dynamic model under high speeds in the closed pipe should be evaluated using FSI, which can provide strong technical support for the design of the maglev flight wind tunnel flow control system. From this, a maglev flight wind tunnel design scheme and dynamic model test method for the capacity can be constructed.

The FSI simulation for the moving body in the long and closed tunnel is not easy to propose because of the large amount of computation cost. The technique for FSI simulation can be classified into monolithic and partitioned coupling; as for the monolithic FSI simulation, all the equations which govern sub-problems and the interaction between fluid and solid are rendered into a single system, and the accuracy, as well as the computation cost, are high. On the contrary, the two different solvers for the fluid and solid sub-problems are coupled in partitioned, and the one- or two-way data exchange between them must be established, so that in this way, the solvers can be tailored, and the computation cost can be highly reduced. For the FSI problem of the moving body coupling with the surrounding flow in the wind tunnel in this paper, the aim of considering the FSI effect is to better capture the wave propagation induced by the high-speed translation of the solid model, the effect of the fluid on the solid can be neglected, and the contact surface is constant; thus, we could use the one-way partitioned FSI simulation technique to solve the problem.

According to the characteristics of the maglev flight wind tunnel test speed, the simulation conditions were established in response to the actual test requirements of the maglev flight wind tunnel. Using FSI, a space–time conservation element and solution element (CE/SE) theoretical method and zonal coupling technology for the aerodynamic structure that could be used to study the supersonic FSI problem were developed to simulate and analyze the unsteady aerodynamic characteristics of the entire process of acceleration, uniform speed, and deceleration in the closed pipe. The FSI mechanism of

high-speed motion in the closed pipe under the dynamic model was analyzed, and the time–history curve of the disturbed flow field parameters was obtained. The multigrid-distributed calculation based on CFD simulation provided support for the design of a maglev flight wind tunnel flow control system and wave elimination measures.

2. Problem Statement

The maglev flight tunnel designed in this paper consisted of accelerating, constant speed, and decelerating sections. The overall length of the tunnel was 1 km, the acceleration section length was 450 m, the constant speed section length was 150 m, and the diameter was 6 m. In this study, we focused on how the aerodynamics changed in the closed tunnel during the acceleration and constant-speed phases. A simplified schematic of the maglev flight tunnel is shown in Figure 1, with a scaled high-speed train used in railway transportation as the model, The model vehicle was 2.2 m high and 60 m long. The blockage effect for the aerodynamic test in the flight tunnel for the high-speed train was similar to the traditional wind tunnel test, which was chosen as 20%, as shown in Figure 2.

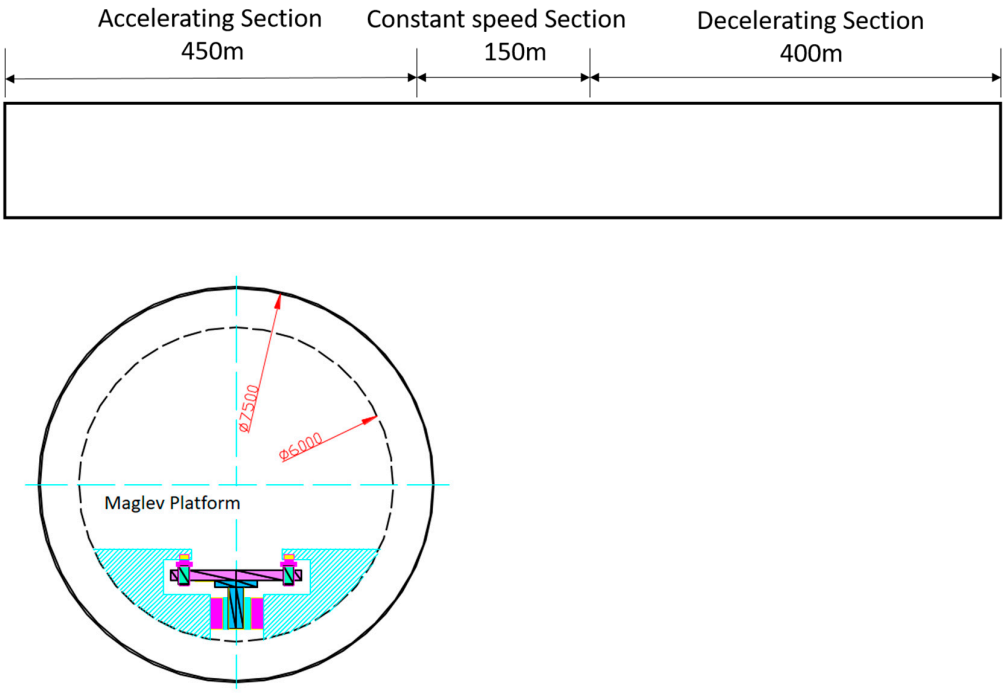


Figure 1. Layout of maglev flight tunnel.

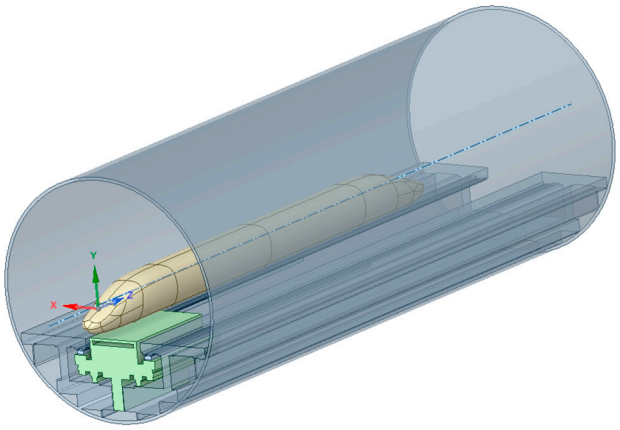


Figure 2. Schematic of high-speed train model and maglev flight tunnel.

3. Methodology

3.1. CE/SE Governing Equations

Unlike the conventional wind tunnel model, the model of the maglev flight wind tunnel is in motion and the fluid medium is in a static state. To analyze the complex pressure wave system generated by the model's movement and the law of the wall, the fluid–structure coupling effect of the model's high-speed motion process was considered. Simultaneously, the maglev flight wind tunnel test model had a transonic supersonic velocity range; therefore, the compressibility of the surrounding flow field was also considered.

CE/SE is a numerical integration method containing high-resolution conservation equations that has emerged in recent years. The model proposed by Chang in 1995 [11] unified time and space and treated them equally. By defining the solution element (SE) and conservation element (CE) using a conservation integral equation, both the local and whole are strictly satisfied by the conservation law [12]. Developed by Zhang et al., this method is used as a new compressible body solution algorithm to solve two- and three-dimensional unsteady Euler equations and has been applied to solve typical multi-physical field coupling problems such as shock waves, aerodynamic noise, and magnetohydrodynamics [13–15].

First, the one-dimensional wave propagation equation is given as follows:

$$\frac{\partial u}{\partial t} + a\frac{\partial u}{\partial x} = 0 \tag{1}$$

where $a > 0$ is the convective term constant. The equation discretizes the element space and generates discrete points at different space positions and given times. The CE/SE method considers time as an additional space coordinate by constructing a two-dimensional Euler space domain and applying the Gaussian divergence theorem in internal time and space. Thus, converting Equation (1) from the differential to the integral form, we obtain [12]:

$$\oint_{S(V)} \vec{h} \cdot d\vec{s} = 0 \tag{2}$$

where *S(V)* is the boundary of any time–space domain, and a unit volume is established in the domain. The unit volume is guaranteed to be conserved locally in time and space and processed uniformly, which is key to constructing the CE. Subsequently, the SE is established such that the variables in the SE unit are sufficiently small to carry out the approximate Taylor series expansion of fluid variables near the inner boundary of the time–space region at the center of a point on the coordinates in the domain.

$$u^*(x,t) = u_q(x,t) + \frac{\partial u_q}{\partial x}(x - x_q) + \frac{\partial u_q}{\partial t}(t - t_q) \tag{3}$$

The time and space derivatives are correlated by the convection–diffusion equation of fluid:

$$u^*(x,t) = u_q(x,t) + \frac{\partial u_q}{\partial x}\left[(x - x_q) - a(t - t_q)\right] \tag{4}$$

The convection–diffusion equation of fluid can then be used to correlate the derivatives of time and space, so that there are only two unknowns and their spatial derivatives.

Finally, to close the system, two CE equations are defined and the convection equation in integral form is obtained, as shown in Equation (2). The CE/SE format can ensure the uniform conservation of SE in time and space. To ensure fluid conservation, time and space integrals are performed along the linear domain formed by CE as follows:

$$\oint_{S(CE^{\pm})} \vec{h}^*_m \cdot d\vec{s} = 0 \tag{5}$$

The solution process can be defined using boundary conditions, including applied pressure, density, temperature, and velocity. Using non-reflective boundary conditions in the treatment of far-field boundary conditions, for the solid wall and reflective boundary conditions, the normal velocity component should be equal and opposite to the incoming velocity, so that the interface velocity is zero. In addition, for the fixed wall boundary, the tangential velocity component should be opposite to the direction of the incoming flow, so that the interface is empty.

As for the thermodynamic considerations in the CESE method we proposed in this paper, the adiabatic expansion of ideal gas is applied. The incremental change in internal energy is dU which could be given by

$$dU = \frac{\rho_0 v_0}{k-1} d\left(\frac{p}{\rho}\right) \tag{6}$$

And integrated to yield

$$e = \frac{U}{\rho_0 v_0} = \frac{p}{\rho(k-1)} \tag{7}$$

Solving for the pressure

$$p = (k-1)\rho e \tag{8}$$

To further analyze the unsteady flow characteristics of the flow field around the model and validate the reliability of the FSI method, the surrounding disturbed flow field was analyzed separately based on the CFD method. Relevant aerodynamic numerical simulation assessments were carried out to provide the basis for a detailed design of the maglev flight tunnel using dynamic mesh technology.

3.2. Fluid Solver

The control equation is a constant Euler/Navier–Stokes (NS) equation group in an arbitrary coordinate system, which can be expressed as follows [16]:

$$\frac{\partial \hat{Q}}{\partial \tau} + \frac{\partial \hat{E}}{\partial \xi} + \frac{\partial \hat{F}}{\partial \eta} + \frac{\partial \hat{G}}{\partial \zeta} = NVIS \cdot \left(\frac{\partial \hat{E}_v}{\partial \xi} + \frac{\partial \hat{F}_v}{\partial \eta} + \frac{\partial \hat{G}_v}{\partial \zeta} \right) \tag{9}$$

where Q is the solution vector and τ is artificial time. The inviscid fluxes in the $\xi-$, $\eta-$, and $\zeta-$directions are E, F and G, and E_v, F_v and G_v are corresponding viscous fluxes. When the above equation is separated using the finite volume method, the following discrete equations are obtained:

$$\frac{V}{\Delta \tau}\delta Q + \omega \left[\frac{\partial}{\partial \xi}(A\delta Q) + \frac{\partial}{\partial \eta}(B\delta Q) + \frac{\partial}{\partial \zeta}(C\delta Q) \right] = RHS \tag{10}$$

$$RHS = -\left(\frac{\partial \hat{E}}{\partial \xi} + \frac{\partial \hat{F}}{\partial \eta} + \frac{\partial \hat{G}}{\partial \zeta}\right)^{(n)} + NVIS \cdot \left(\frac{\partial \hat{E}_v}{\partial \xi} + \frac{\partial \hat{F}_v}{\partial \eta} + \frac{\partial \hat{G}_v}{\partial \zeta}\right)^{(n)} \tag{11}$$

where A, B, and C are the Jacobian matrices of flows in three directions, $\delta Q = Q^{(n+1)} - Q^{(n)}$, and $V = 1/J$. $\omega = 1$ represents the first order accuracy of the time direction, whereas $\omega = 1/2$ represents the second order.

The lower-upper symmetric Gauss–Seidel method was used to discretize the left of the equation, whereas the MUSCL–Roe scheme was used to discretize the right of the equation. MUSCL–Roe has low format stickiness and high numerical accuracy; therefore, it is suitable for fine simulations of complex flows. For the flux splits, Roe's flux differential split was used. The solution format was in a full and second-order upwind format.

3.3. Turbulent Model

The widely used turbulence model, a two-equation model of Menter's k-Omega shear stress transport (SST) [17,18], was used in this paper. The calculation was mainly based on the SST two-equation model. The SST model was obtained by Menter to further enhance the computational capacity of the strong reverse pressure gradient separated flow. The control equations were as follows:

$$\frac{Dk}{Dt} = \frac{1}{\rho}P_k - \beta' k\omega + \frac{1}{\rho}\frac{\partial}{\partial x_i}\left[\left(\mu + \frac{\mu_t}{\sigma_k}\right)\frac{\partial k}{\partial x_i}\right], \tag{12}$$

$$\frac{D\omega}{Dt} = \frac{1}{\rho}P_\omega - \beta\omega^2 + \frac{1}{\rho}\frac{\partial}{\partial x_i}\left[\left(\mu + \frac{\mu_t}{\sigma_\omega}\right)\frac{\partial \omega}{\partial x_i}\right] + 2(1-F_1)\sigma_{\omega_2}\frac{1}{\omega}\frac{\partial k}{\partial x_i}\frac{\partial \omega}{\partial x_i}, \tag{13}$$

$$\mu_t = \min\left[\rho k/\omega, \frac{a_1\rho k}{\Omega F_2}\right], \tag{14}$$

where k and ω are the quantity of Wilcox's $k-\omega$ model, ρ is density, ρ is viscosity, $a_1 = 0.31$ is a model constant, $\beta = 0.09$ is a model constant, and F_1, F_2 a blending function given in Ref. [19]. For the boundary conditions, no-slip velocity conditions were used on the solid body surface. The computing grid was created using the splicing method, and the splice boundary conditions were used to deliver the values of the splice face. The inlet and outlet were defined as the pressure boundary. The models operated at a Mach number of 0.5.

4. Numerical Simulation

4.1. FSI Platform

For the aerodynamic–structure coupling problem, the fluid and structure solvers must be solved uniformly, information transfer variables found, and coupling platform established. Here, the CE/SE and structural dynamics algorithms can be coupled to realize the aerodynamic–structure coupling simulation of the high-speed motion process. Since the two algorithms can be calculated independently, the flow field and structure can be meshed, and the time step set separately. The coupling system automatically tracks the minimum time step in the two domains for calculation. The aerodynamic–structure coupling process requires the Lagrange structure to be embedded in the fluid domain and the node displacement and velocity information to be transferred to the fluid solver in each time step. During the initial solution time step, the CE/SE algorithm first uses the initial velocity and pressure to solve the compressible flow field and obtain the interface pressure. Then, the pressure is applied to the structure domain as the boundary condition. After solving the structure domain, the displacement and velocity of the node are obtained, and the displacement and velocity of the boundary node are returned to the fluid field so that the fluid and structure enter the convergence iteration process. When the convergence conditions are satisfied, the next time step is calculated. The specific fluid–structure coupling iterative process of the whole system is shown in Figures 3 and 4.

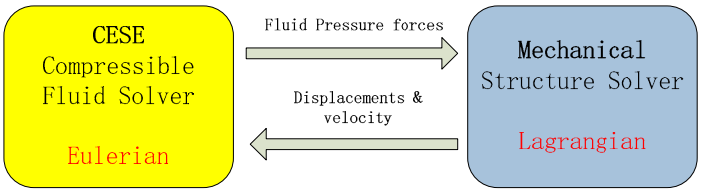


Figure 3. Fluid structure interaction platform.

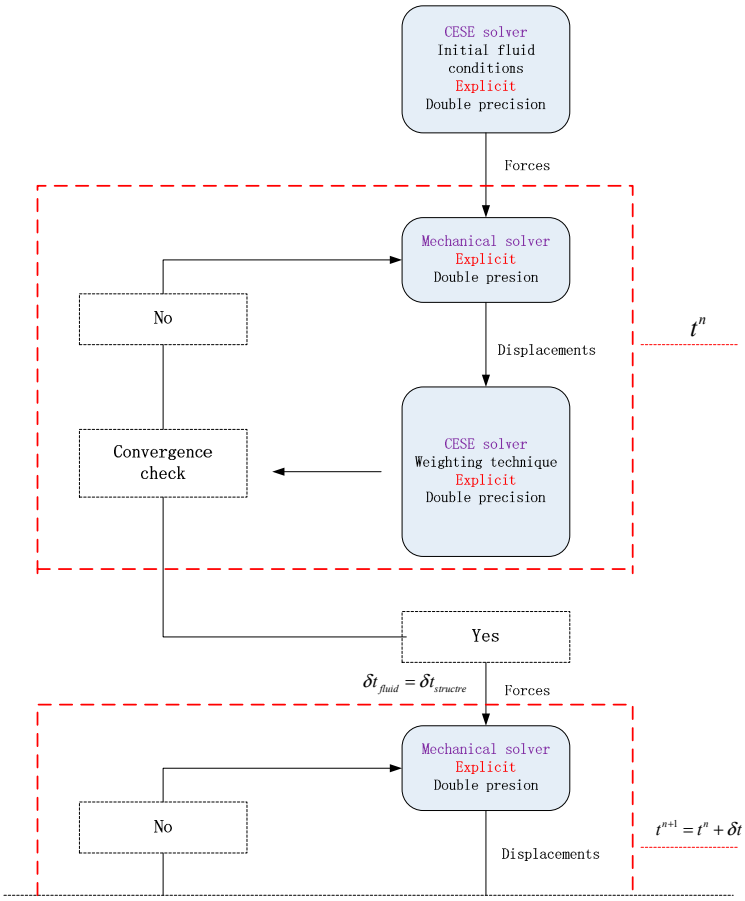


Figure 4. Flowchart to solve fluid structure interaction based on conservation element and solution element algorithm [20].

4.2. FSI Modelling

The structural finite element model was mainly composed of the maglev flying wind tunnel platform and test model. The fluid model schematic diagram is shown in Figure 4. The length of the fluid grid field was 1000 m. According to the characteristics of the CE/SE coupling solution algorithm, a structured grid was adopted for the flow field with a minimum grid size of 0.01 m. We assumed that the platform and structural models had no deformation and were made of rigid materials.

4.3. FSI Simulation and Results

Two simulation conditions were established according to the maglev flight wind tunnel test conditions. The total length of the pipeline was 1000 m, divided into acceleration, uniform speed, and deceleration or braking sections. The maximum speed of working condition 1 was 170 m/s and that of working condition 2 was 340 m/s. Both the acceleration and deceleration were uniform. The specific condition parameters are shown in Table 1. Gravity was considered in all the simulation conditions. The model simulated a test plugging ratio of 20%, that is, the resistance area of the model movement process accounted for 20% of the available area of the pipeline cross section.

Table 1. List of fluid structure interaction simulation conditions.

Case	Moving Velocity (m/s)	Static Pressure (Pa)	Density (kg/m^3)
No. 1	170	101,325	1.25
No. 2	340	101,325	1.25

A total of five cross sections with longitudinal positions of 0, 450, 500, 600, and 1000 m inside the wind tunnel pipe were obtained, and the time-varying curves of pressure on the cross sections under the movement process of the closed pipe were the output. The results of each cross section under working condition 1 are shown in Figure 5. The 450, 500, and 600 m cross sections exhibited two peak pressure wave values. The first pressure wave arrived a little earlier than the motion model at the selected cross section. The speed at the head of the compression wave was significantly faster than the model movement speed, fell sharply after the peak, and then increased slowly. After the compression wave generated at the head of the model moved through a cross section, the expansion wave generated at the tail reappeared at the same cross section. The second wave peak existed simultaneously to the deceleration of the model, which was the moment when the compression wave generated by the model movement met the reflected wave generated by the end wall of the pipe and moved to the cross section. The cross section at the end of the pipe at 1000 m exhibited only one wave peak, which appeared in the deceleration phase of the model.

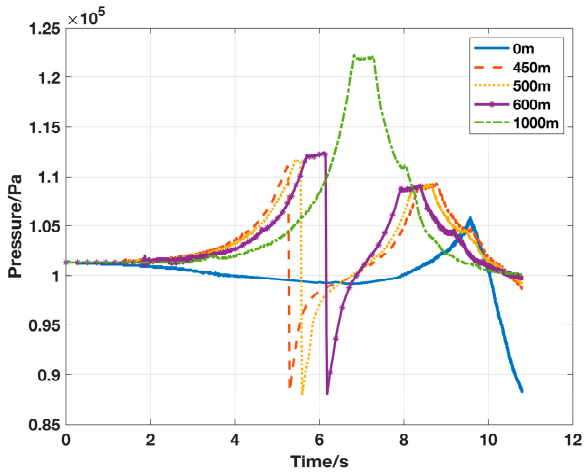


Figure 5. Time–history curves for pressures on corresponding sections of tunnel in working condition 1.

The results of each cross section in working condition 2 are shown in Figure 6. The pressure curve variation rule shows that the 450, 500, and 600 m cross sections exhibited similar pressure waves to those of working condition 1. However, the 1000 m cross section at the end of the pipeline experienced multiple peak values, which could be the result of multiple pressure waves on the end wall.

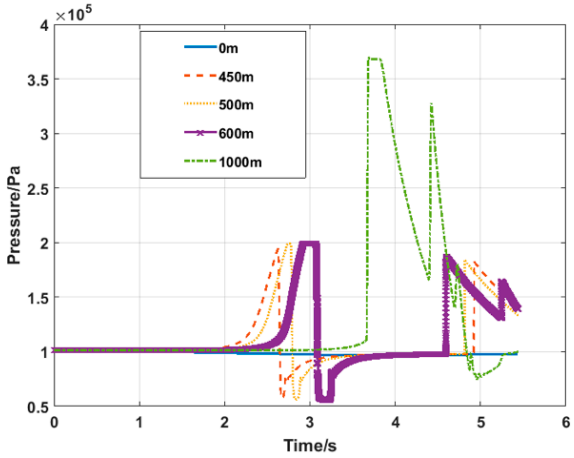


Figure 6. Time–history curves for pressures on corresponding sections in tunnel for working condition 2.

Combined with the time-varying pressure wave curves in the model movement process of the two working conditions, and compared with the time-varying curves of the model movement velocity, we found that, when the model was running at a uniform speed in the test section, the pressure waves at the cross section in the test section had fluctuation peaks, which is not conducive to carrying out aerodynamic tests. In addition, the triggers for the time movement speed pass show no significant effect on the wave propagation for both conditions. Therefore, it is necessary to take measures to suppress the pressure wave generated by the high-speed movement of the model in the test section.

Figures 7 and 8 show working conditions 1 and 2, respectively, as the aerodynamic changes over time. The case with a maximum model speed of Mach 0.5 showed that the aerodynamic drag was at a constant speed in the acceleration section with no obvious changes, and the deceleration period had a maximum resistance of 1.1 times the lowest resistance. At the maximum speed of Mach 1.0, the aerodynamic resistance of the moving model began to decrease slightly and reached the minimum in the deceleration stage, with the peak value of aerodynamic resistance about twice that of the earlier stages. Both the variations in the drag curves for the two conditions show periodic fluctuations at Mach 0.5; this phenomenon occurs during the acceleration period, while for Mach 1.0, the periodic fluctuation shows during the deceleration period. This difference is mostly correlated with the wave propagation speed.

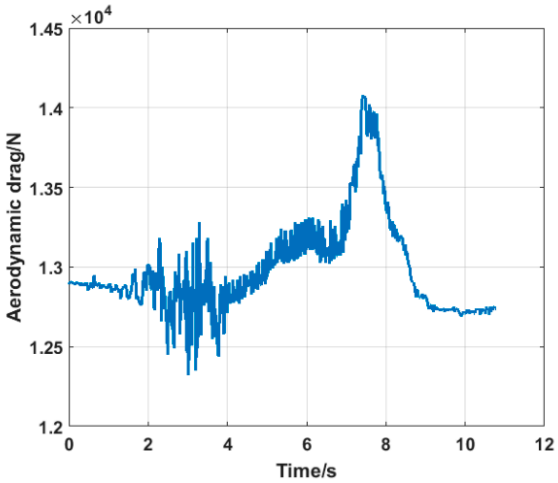


Figure 7. Time–history curves for aerodynamic drag under moving model in working condition 1.

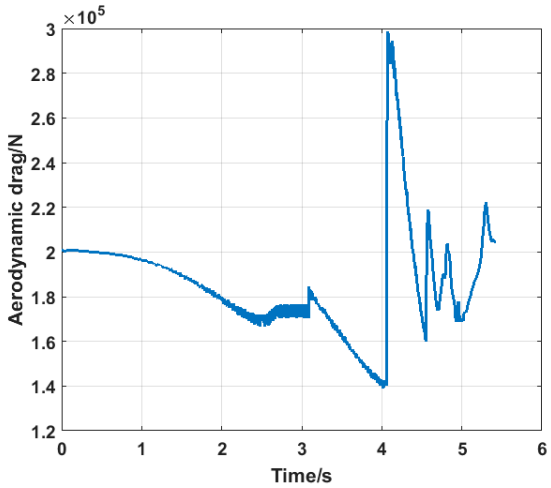


Figure 8. Time–history curves for aerodynamic drag under moving model in working condition 2.

Figures 9 and 10 are three-dimensional velocity cloud diagrams and the Schlieren number results of the unsteady flow field evolution in the acceleration, uniform-speed, and deceleration processes of the model in a straight, closed pipe. The propagation process of the wave system in the high-speed motion process of the model in the pipe can be clearly seen in the figure. The forward moving speed of the wave front was significantly faster than that of the model. Therefore, when the model does not reach the end of the pipe, the wave front reaches the wall ahead of the model and produces a reflection.

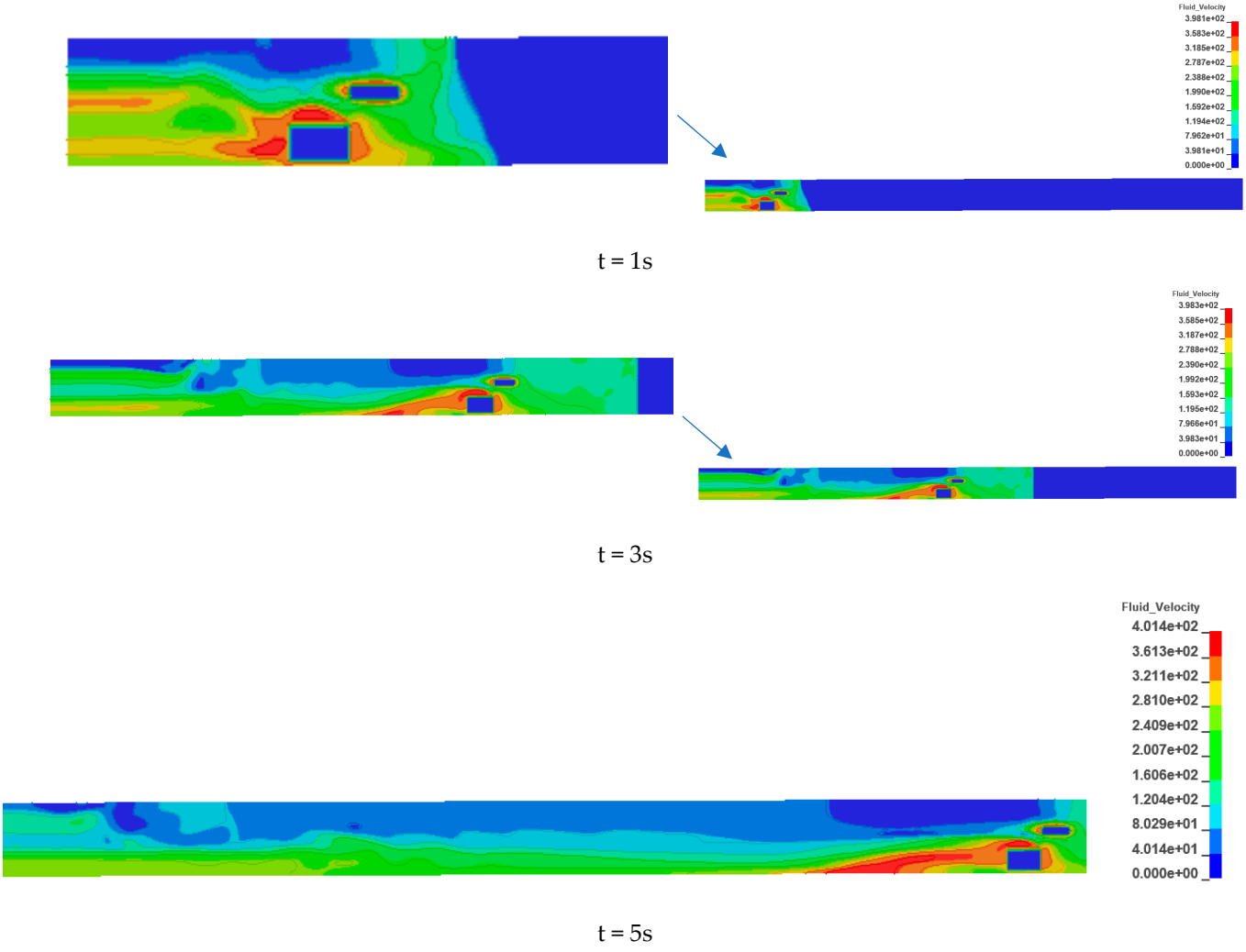


Figure 9. Velocity contours at different times under moving model for Mach 1.0.

4.4. CFD Validation

4.4.1. Parallel Multigrid Algorithm and Train Movement

The parallel approach uses an area decomposition method for data division. Based on the number of processors, the entire computational area (computational grid) is automatically divided into several sub-areas during the pre-processing process. This means that the computing grid is divided evenly into a number of separate parts, and each is assigned to separate processors. The initial flow field parameters or the geometric parameters of the corresponding sub-area are loaded into each processor to initiate the computational process. During each full-scale scan, each processor completes the calculation of the corresponding sub-areas and transfers the functions library by calling messages to exchange the data in the area boundary. The data on the flow field calculation results are retained for each area. One of these processes, referred to as root processes, is responsible for the collection of the full-field residual data, processing of the time statistics, discrimination of the convergence

criterion, broadcasting of convergence messages, analysis of parallel efficiency, and merging of the flow field.

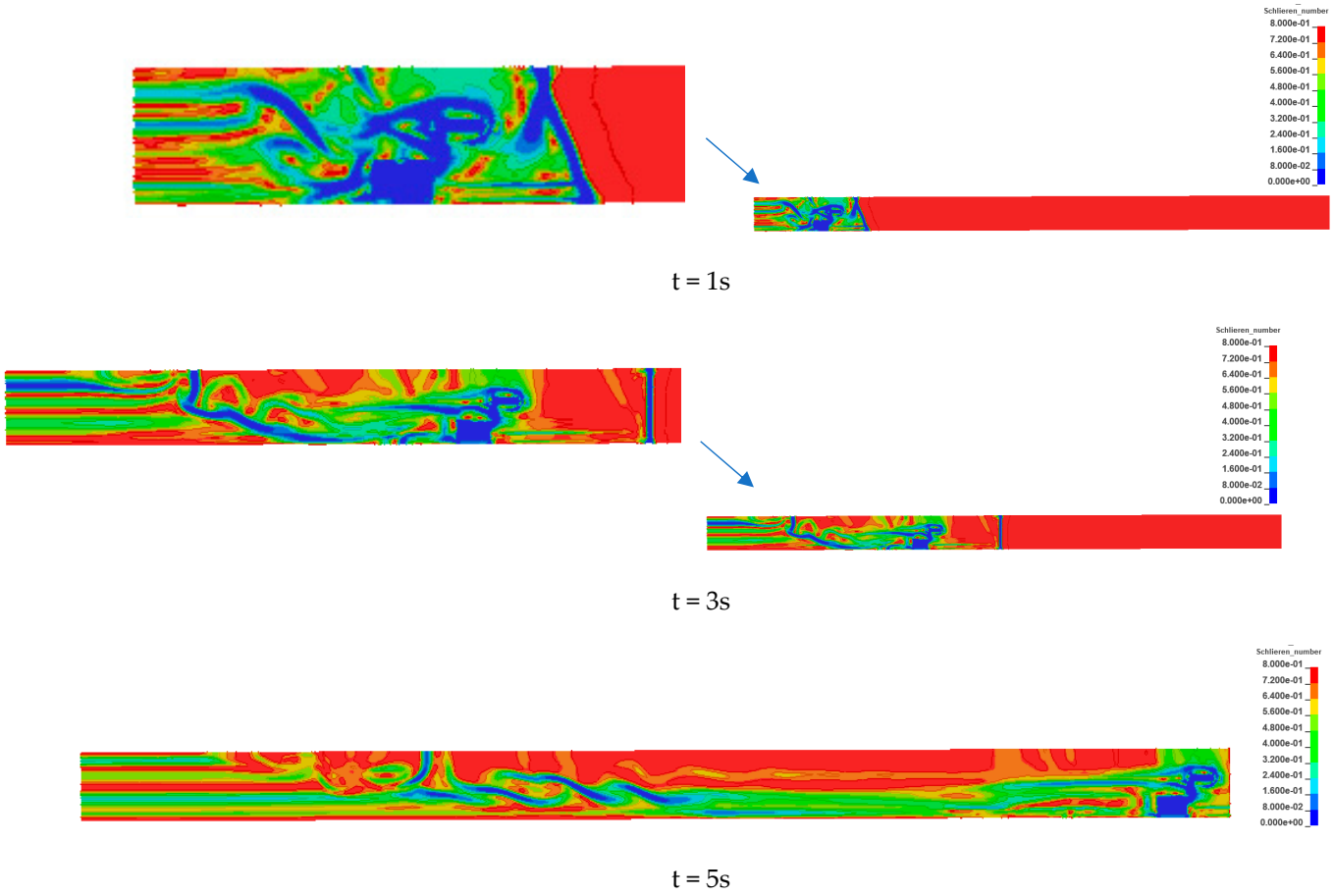


Figure 10. Schlieren distribution contours at different times under moving model for Mach 1.0.

Multigrid techniques are used in calculations to accelerate the convergence of the flow field calculation. In 1977, Brandt first applied multigrid technology to solve discrete forms of non-linear differential equations. Since then, this method has been increasingly used to solve discrete equations in flow and heat exchange problems [21–23]. With the development of other numerical methods, the multigrid technique has made great progress. Many numerical experiments have shown that the multigrid technique, when applied rationally, tends to raise the rate of convergence of steady flow calculation by one or two scales, which is currently recognized as one of the most effective methods of acceleration.

During the Euler/NS equation solution process, high-frequency errors can be eliminated quickly and simultaneously in the iterative solution using error analysis, whereas the elimination speed of low-frequency errors is much slower, significantly decreasing the convergence rate of the flow field. The idea of the multigrid is to use a series of increasingly thick grids to quickly eliminate high-frequency errors on various layers of grids to accelerate the convergence. Low-frequency errors that cannot be eliminated on the densest grid become high-frequency errors on the thick grid, which are easy to eliminate. As a result, the iteration between different-density grids can quickly eliminate all frequency errors on the densest grid layer for a rapid convergence of the flow field. For moving grid models, dual-grid technology was applied to mesh the wind tunnels and model.

The train movement could be realized by the parallel multigrid algorithm presented above; here, we give the prescribed moving velocity curve for the train model at different conditions, including uniformly accelerated motion and uniform motion.

4.4.2. CFD Modelling

To analyze the true aerodynamic properties of the calculation model with a blockage of 20%, the calculation considered the entire tunnel, which was 500 m long and 6.0 m in diameter. The model vehicle was 2.2 m high and 60 m long, as shown in Figure 11.

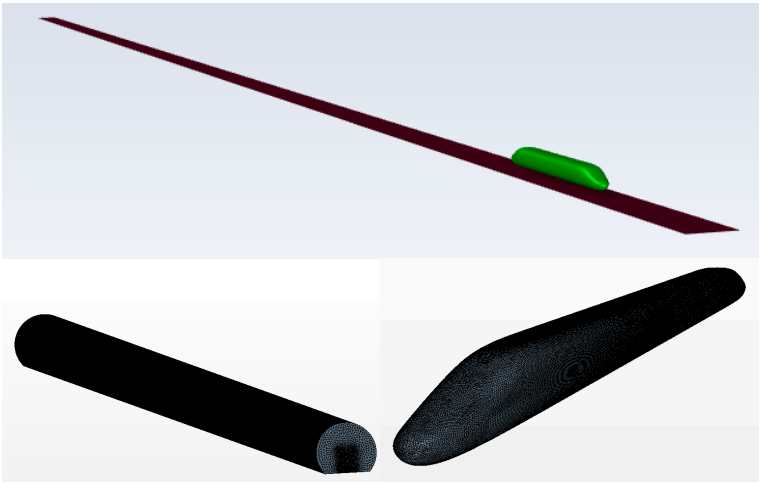


Figure 11. Grid of vehicle model and wind tunnel with blockage of 20%.

The vehicle model and wind tunnel used non-structural grids. To ensure numerical accuracy, the boundary layer needed to be generated on the surface of the vehicle model, which contained a four-story boundary layer. The vehicle model area combined with the tunnel was processed using interpolation with a moving grid. The computational model with 20% blockage had an overall computing grid of approximately 65 million. The central-area grids of the flow field and vehicle models were properly refined. These area grids are shown in Figure 11.

4.5. Validation Results and Comparison

The aerodynamic properties of the model such as the speed, pressure, and vortex were calculated and displayed in distribution clouds, as shown in Figures 12–14. For models with a blockage of 20%, the blocking effect during the model movement was evident. From the numerical simulation results, the test vehicle model had a relatively weak tail flow and tail vortex when it moved in the maglev flight tunnel. In working condition 1 with a speed of 170 m/s, the tail flow was approximately 15 m long during the acceleration phase, as shown in Figure 13. On the surface and vicinity of the test vehicle model, the static pressure distribution pattern was similar to that of the vehicle model in a conventional wind tunnel, with higher pressure distributed at the front and end of the model, and lower pressure distributed at the middle of the model, as shown in Figure 14.

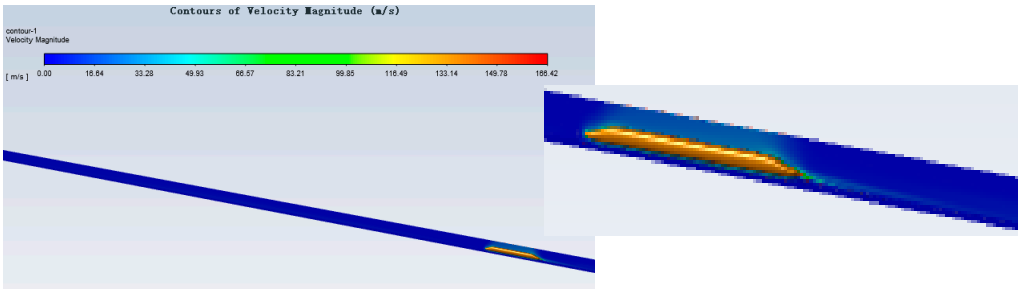


Figure 12. Distribution of speed.

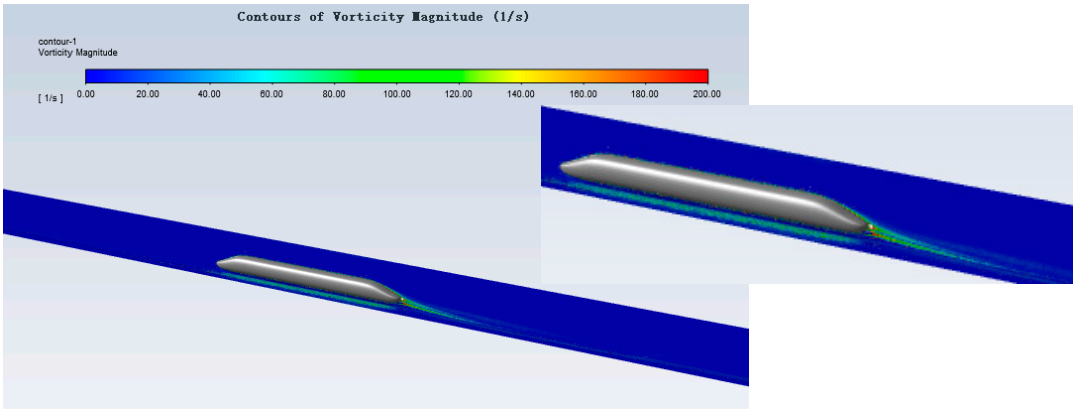


Figure 13. Distribution of vortex.

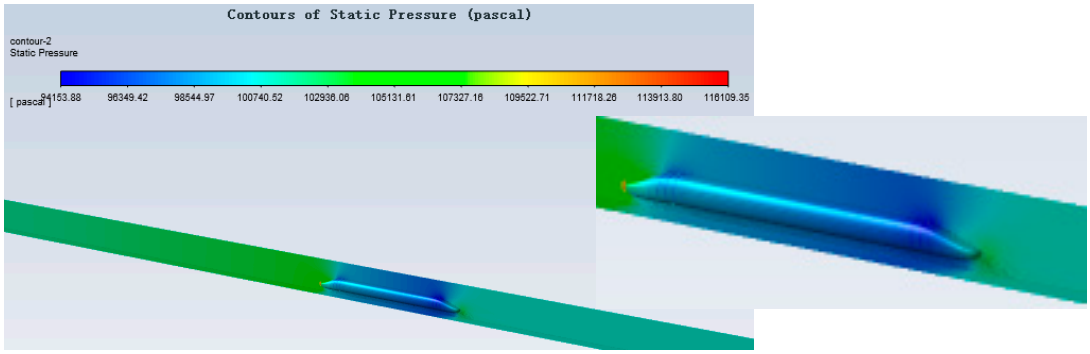


Figure 14. Distribution of static pressure.

On the tunnel wall in front of the dynamic test vehicle model, a higher static pressure area was created. However, the pressure difference in these two areas was relatively large: approximately 5000 Pa between the high- and low-pressure areas, as shown in Figure 15.

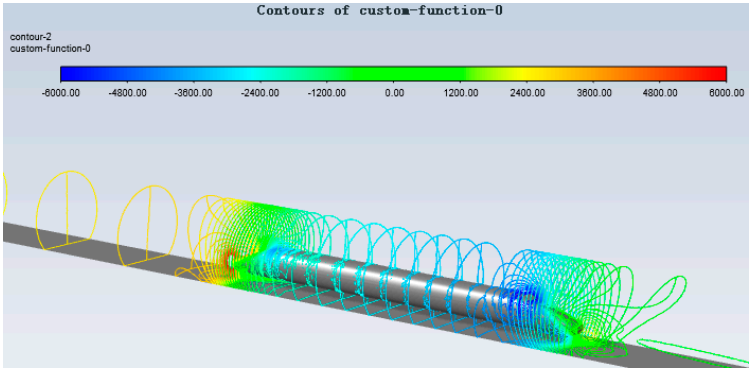


Figure 15. Distribution of static pressure pulsation.

When the blockage of the model was large, the fluctuating pressure coefficient of the strength of the compressed wave in front of the model was 14.4% relative to the dynamic pressure of the model, which was much higher than that of a smaller blockage model. Therefore, the intensity of the disturbance wave needs to be contained.

When the wind tunnel was in use, the compression wave, expansion, and airflow disturbance caused by the high-speed movement of the model were reflected in the tunnel body, presenting different pressure states at different positions. To study the dynamic aerodynamic characteristics of the gas in the pipe caused by the movement of the model car,

the flow field in the pipe at different times was recorded and analyzed, and the axial static pressure distribution at the top of the pipe wall at different times is shown in Figure 16.

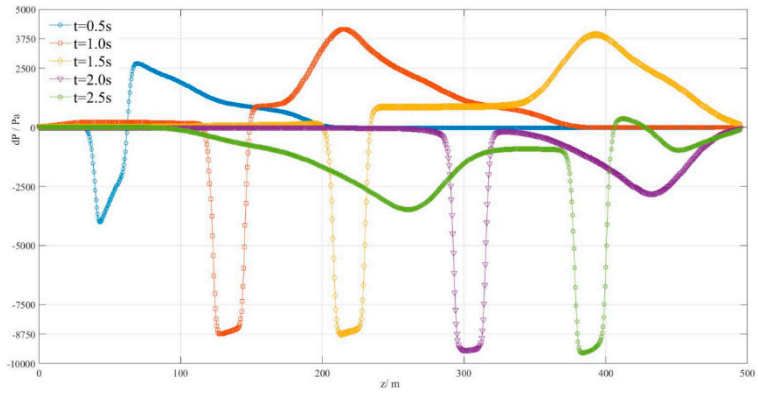


Figure 16. Static pressure distribution on tunnel wall at different times.

The results show that, during the high-speed motion of the vehicle model at Mach 0.5, the compressed wave in front of the model was moving forward and away from the model. The compressed wave caused a rise in the wall pressure of approximately 4000 Pa. The static pressure around the model was low, at approximately 10,000 Pa below the ambient pressure of the wind tunnel. The increase in pressure caused by the expansion wave at the back of the model was minimal.

The comparison results of the pressure, as well as drag, along the wind tunnel during train movement for condition 1 between FSI and CFD simulations are listed in Table 2; it can be seen from the comparison results that the CFD aerodynamics are close to the FSI simulation, which provide a good support for the FSI simulation, while the overall CFD results are smaller than the FSI results, so that perhaps the disturbance of the solid effect on the fluid needs to be considered as the FSI simulation did. Furthermore, for the velocity distribution of Figure 10, the high region is around the model, which is coincident with the corresponding pressure distribution of the CFD in Figures 14 and 15. All in all, the tail region of the model needs to be more carefully considered.

Table 2. Comparing results between FSI and CFD simulation.

Time (s)	Simulation	Pressure (Pa)	Error	Drag (N)	Error
4	FSI	102,445	1.58%	12,870	4.8%
	CFD	100,826		12,252	
5	FSI	107,754	1.92%	13,100	2.02%
	CFD	105,682		12,835	
6	FSI	97,680	5.26%	13,250	1.49%
	CFD	92,543		13,052	
8	FSI	106,652	2.09%	13,410	0.95%
	CFD	104,421		13,283	
10	FSI	101,345	0.68%	12,710	1.27%
	CFD	100,652		12,548	

5. Conclusions

Based on the CE/SE fluid–structure coupling method, an aerodynamic–structure coupling simulation of the high-speed movement process of a moving model in a pipeline was carried out. For each working condition, we modelled the convergence and obtained a complete dynamic model of the motion process of the flow field. Simulation results

were used to evaluate the modelled aerodynamic properties in the pipeline and pressure wave propagation in the movement process. Finally, using the CFD method, we further verified the reliability of the unsteady-flow dynamic characteristic calculation results. The results provide a theoretical basis for the design of a pipeline flow control system. The fluid–structure coupling method can be used to evaluate the unsteady aerodynamic characteristics of the dynamic model moving at high speeds in a closed pipe from the perspective of aerodynamic–structure coupling.

Author Contributions: Conceptualization, C.F.; methodology, X.G.; FSI modeling, J.K.; CFD validation, Y.S.; Result analysis, D.X. and J.C.; project administration, C.F.; funding acquisition, C.F. All authors have read and agreed to the published version of the manuscript.

Funding: This research was funded by National Natural Science Foundation of China, grant number 11902331, 91530319 and 11325212.

Institutional Review Board Statement: Not applicable.

Informed Consent Statement: Not applicable.

Data Availability Statement: Not applicable.

Conflicts of Interest: The authors declare no conflict of interest.

References

1. Liu, Z. *Wind Tunnel Construction Design*; China Astronautic Publishing House: Beijing, China, 2005.
2. Buntov, M.Y.; Makeev, P.V.; Ignatkin, Y.M.; Glazkov, V.S. Numerical Modeling of the Walls Perforation Influence on the Accuracy of Wind Tunnel Experiments Using Two-Dimensional Computational Fluid Dynamics Model. *Aerospace* **2022**, *9*, 478. [CrossRef]
3. China Aerodynamics and Development Center. *Proposal for Construction Project of Maglev Flight Wind Tunnel*; China Aerodynamics and Development Center: Mianyang, China, 2019.
4. Ni, Z.; Zhang, J.; Fu, C.; Wang, B.; Li, Y. Analyses of the test techniques and applications of maglev flight tunnels. *Acta Aerodyn. Sin.* **2021**, *39*, 95–110.
5. Liu, J.; Zhang, J.; Weihua, Z. Analysis of Aerodynamic Characteristics of High-speed Trains in the Evacuated Tube. *J. Mech. Eng.* **2013**, *49*, 7. [CrossRef]
6. Nakata, D.; Yasuda, K.; Horio, S.; Higashino, K. A fundamental study on the hybrid rocket clustering for the rocket sled propulsion system. In Proceedings of the 52nd AIAA/SAE/ASEE Joint Propulsion Conference, Salt Lake City, UT, USA, 25–27 July 2016; AIAA: Reston, VA, USA, 2016.
7. Tian, H. Study Evolvement of Train Aerodynamics in China. *J. Traffic Transp. Eng.* **2006**, *6*, 1–9.
8. Zhang, X.; Li, T.; Zhang, J.; Zhang, W. Aerodynamic Choked Flow and Shock Wave Phenomena of Subsonic Evacuated Tube Train. *J. Mech. Eng.* **2021**, *57*, 182–190.
9. Lofftus, D.; Lund, T.; Rote, D.; Bushnell, M.D. *High-Lift Flight Tunnel—Phase II Report*; NASA: Washington, DC, USA, 2000.
10. Zhou, Y.; Chang, X.; Yi, S. The aerodynamic and structural design of low turbulence intensity of MSWT. *Exp. Meas. Fluid Mech.* **2001**, *15*, 1–6.
11. Chang, S.C. The Method of Space-Time Conservation Element and Solution Element—A New Approach for Solving the Navier-Stokes and Euler Equations. *J. Comput. Phys.* **1995**, *119*, 295–324. [CrossRef]
12. Zhang, Z.C.; Yu, S.; Chang, S.C. A Space-Time Conservation Element and Solution Element Method for Solving the Two- and Three-Dimensional Unsteady Euler Equations Using Quadrilateral and Hexahedral Meshes. *J. Comput. Phys.* **2002**, *175*, 168–199.
13. Jiang, Y.; Wen, C.-Y.; Zhang, D. Space–Time Conservation Element and Solution Element Method and Its Applications. *AIAA J.* **2020**, *58*, 5408–5430. [CrossRef]
14. Siavashi, M.; Pourafshary, P.; Raisee, M. Application of space-time conservation element and solution element method in streamline simulation. *J. Pet. Sci. Eng.* **2012**, *96–97*, 58–67. [CrossRef]
15. Chang, S.C.; Wang, X.Y.; To, W.M. Application of the Space–Time Conservation Element and Solution Element Method to One-Dimensional Convection–Diffusion Problems. *J. Comput. Phys.* **2000**, *165*, 189–215. [CrossRef]
16. Hajihassanpour, M.; Hejranfar, K. A High-order nodal discontinuous Galerkin method to solve preconditioned multiphase Euler/Navier-Stokes equations for inviscid/viscous cavitating flows. *Int. J. Numer. Methods Fluids* **2020**, *92*, 478–508. [CrossRef]
17. Shah, M.Z.M.; Basuno, B.; Abdullah, A. Comparative Study on Several Type of Turbulence Model Available in ANSYS-Fluent Software for ONERA M6 Wing Aerodynamic Analysis. *J. Adv. Mech. Eng. Appl.* **2020**, *1*, 9–19.
18. Bing, C.; Xu, X.; Baoxi, W.; Yan, Z. Numerical simulations of turbulent flows in aeroramp injector/gas-pilot flame scramjet. *Chin. J. Aeronaut.* **2017**, *30*, 1373–1390.
19. Menter, F.R. Two-equation eddy-viscosity turbulence models for engineering applications. *AIAA J.* **1994**, *32*, 1598–1605. [CrossRef]
20. Gao, X.L. Research on Multibody Dynamics and Fluid-Structure Interaction of Parachute-Body System. Ph.D. Thesis, National University of Defense Technology, Changsha, China, 2016.

21. Chan, T.F.; Schreiber, R. Parallel Networks for Multi-Grid Algorithms: Architecture and Complexity. *SIAM J. Sci. Stat. Comput.* **1985**, *6*, 698. [CrossRef]
22. Guo, Q.; Paker, Y.; Zhang, S.; Parkinson, D.; Wei, J. Optimum tactics of parallel multi-grid algorithm with virtual boundary forecast method running on a local network with the PVM platform. *J. Comput. Sci. Technol.* **2000**, *15*, 355–359. [CrossRef]
23. Al-Mahdawi, H.K.I.; Abotaleb, M.; Alkattan, H.; Tareq, A.-M.Z.; Badr, A.; Kadi, A. Multigrid Method for Solving Inverse Problems for Heat Equation. *Mathematics* **2022**, *10*, 2802. [CrossRef]

Disclaimer/Publisher's Note: The statements, opinions and data contained in all publications are solely those of the individual author(s) and contributor(s) and not of MDPI and/or the editor(s). MDPI and/or the editor(s) disclaim responsibility for any injury to people or property resulting from any ideas, methods, instructions or products referred to in the content.